Available online at www.sciencedirect.com
ScienceDirect
Trans. Nonferrous Met. Soc. China 33(2023) 997−1014
Transactions of Nonferrous Metals Society of China
www.tnmsc.cn

Thermodynamic modeling and solidified microstructure of Ag–Sn–Zr ternary system

Yu ZHANG[1], Biao HU[1], Yu-chao SHI[1], Shu-hong LIU[2], Yong DU[2], Jie-qiong HU[3]

1. School of Materials Science and Engineering, Anhui University of Science and Technology, Huainan 232001, China;
2. State Key Laboratory of Powder Metallurgy, Central South University, Changsha 410083, China;
3. Sino-Precious Metals Holding Co., Ltd., Kunming 650000, China

Received 20 November 2021; accepted 3 March 2022

Abstract: The phase equilibria of the Ag−Sn−Zr ternary system were investigated over the whole composition via thermodynamic modeling coupled with key experiments. Twenty-two equilibrated alloys were prepared to determine the isothermal sections of the Ag−Sn−Zr system at 500, 700 and 900 °C by means of X-ray diffraction (XRD) and scanning electron microscopy with energy dispersive X-ray spectroscopy (SEM/EDS), and eight as-cast alloys were prepared to study the solidification behavior of the alloys. The solubilities of Zr, Sn and Ag in binary compounds of the Ag−Sn, Ag−Zr and Sn−Zr systems were measured. No ternary compound was found. Based on the thermodynamic descriptions of three constitutive binary systems as well as the experimental phase equilibria data obtained from the present work, thermodynamic assessment of the Ag−Sn−Zr system was carried out by the CALPHAD (Calculation of phase diagrams) approach. A set of thermodynamic parameters of the Ag−Sn−Zr system were obtained. The calculated isothermal sections are in good agreement with most of the reliable experimental data. The liquidus projection and reaction scheme of the Ag−Sn−Zr system over the whole composition were also presented. The solidification behaviors of as-cast alloys were simulated under Gulliver−Scheil non-equilibrium condition. The simulated and experimental results are consistent with each other.

Key words: Ag−Sn−Zr system; phase equilibria; thermodynamic modeling; microstructure; solidification simulation

1 Introduction

The Ag−Sn−Zr system is of great technical importance both as Ag-based and Zr-based alloys. On the one hand, Ag-based alloys are extensively utilized in electronic industry, mechanical brazing and reflected backing for optics railways as they display high strength brazing, excellent electronic properties, thermal conductivity and process performance [1−3]. It was reported that a small addition of Sn and Zr in Ag-alloys leads to a considerable enhancement of strength, electrical and mechanical properties in the fabrication process through solid solution strengthening and precipitation hardening mechanisms [4−6]. For instance, TAHER et al [5] reported Sn as alloying element to improve the strength and mechanical properties of Ag-alloys due to the formation of the Ag_3Sn and hcp(AgSn) phases. On the other hand, there is extensive application of Zr-based alloys in the field of the nuclear industry as fuel cladding material due to low neutron absorption coefficient, good processing properties and superior corrosion resistance [7,8]. The addition of Ag in Zr-based alloys can improve their glass forming ability and crystallization kinetics [9−11]. Investigation by YANG et al [11] reveals that 2 at.% Ag in Zr-based bulk metallic glasses brings about high ultimate fracture strength and plastic strain, which is caused

Corresponding author: Biao HU, Tel/Fax: +86-554-6601194, E-mail: hubiao05047071@163.com
DOI: 10.1016/S1003-6326(23)66161-8

by the atomic size mismatch of Ag with Zr and the formation of eutectic structure. Knowledge of the phase equilibria and thermodynamic properties of the Ag−Sn−Zr system is essential in developing new Ag-based and Zr-based high-temperature structural materials. Consequently, the phase equilibria of the Ag–Sn–Zr system play a significant role in improving the thermal and mechanical properties of Ag-based and Zr-based alloys.

Therefore, the purposes of the present work are: (1) to determine the isothermal sections at 500, 700 and 900 °C via techniques including XRD and SEM/EDS; (2) to obtain an optimal set of reliable thermodynamic parameters for the ternary system over the entire composition by the CALPHAD approach [12,13]; (3) to experimentally investigate the solidified microstructure of the Ag–Sn−Zr system; (4) to perform the Scheil solidification simulations and calculate the reaction scheme for the ternary system using the presently-established thermodynamic parameters. The investigations on phase equilibria and solidified microstructure of the Ag−Sn−Zr system are anticipated to provide a new insight in establishing thermodynamic database of multicomponent Ag-based and Zr-based alloys.

2 Evaluation of literature data

Solid phases [14] with their crystal structures in the Ag−Sn−Zr system are summarized in Table 1.

2.1 Ag−Sn binary system

The phase equilibria and thermodynamic properties of Ag–Sn system have been investigated by many researchers [21−25]. The existence of the intermediate phases, i.e., hcp(AgSn) and Ag_3Sn, in the Ag–Sn system was determined and confirmed by PETRENKO [21], PUSHIN [22] and MURPHY [23] using XRD and micrographic analysis methods, and Ag_3Sn phase was reported to be homogeneous between 23.7 and 25 at.%. Though KARAKAYA and THOMPSON [26] reproduced overall features of the phase diagram and individual phases using CALPHAD method, they modeled the Ag_3Sn phase as a simple substitutional solid solution and did not employ the lattice stability values of pure elements recommended by the SGTE database [27]. Later, CHEVALIER [15] attempted to revise the result from KARAKAYA and THOMPSON [26] within the framework of SGTE description and update the thermodynamic description of Ag–Sn system. However, the thermodynamic parameters from CHEVALIER [15] couldn't reproduce well the invariant reaction of Liquid + (Ag) → hcp(AgSn) at 724 °C. KATTNER and BOETTINGER [16] also optimized the limited model parameters. However, the calculation couldn't satisfy the thermochemical properties of the solid phases, such as enthalpies of formation and heat capacities. Then, a more recent thermodynamic assessment of the Ag–Sn system has been performed by OH et al [28], and it can

Table 1 Solid phases in Ag–Sn–Zr system

Phase	Prototype	Personal system	Space group	Lattice parameter/nm			Ref.
				a	*b*	*c*	
(Ag)	Cu	*cF*4	$Fm\bar{3}m$	4.071	4.071	4.071	[14]
(*α*Sn)	C(d)	*cF*8	$Fd\bar{3}m$	6.489	6.489	6.489	[14]
(*β*Sn)	*β*Sn	*tI*4	$I4_1/amd$	5.833	5.833	3.182	[14]
(*α*Zr)	Mg	*hP*2	$P6_3/mmc$	3.232	3.232	5.148	[14]
(*β*Zr)	W	*CI*2	$Im\bar{3}m$	3.616	3.616	3.616	[14]
Ag_3Sn	Cu_3Ti	*oP*8	*Pmmn*	5.968	4.780	5.184	[15]
hcp(AgSn)	Mg	*hP*2	$P6_3/mmc$	2.966	2.966	4.782	[16]
AgZr	CuTi	*tP*4	*P4/nmm*	3.468	3.468	6.603	[17]
$AgZr_2$	$CuZr_2$	*tI*6	*I4/mmm*	3.246	3.246	12.004	[18]
$ZrSn_2$	$TiSi_2$	*oF*24	*Fddd*	9.573	5.644	9.927	[19]
Zr_5Sn_3	Ti_5Ga_3	*hP*18	$P6_3/mcm$	8.460	8.460	5.780	[19]
Zr_4Sn	W_3O	*cP*8	$Fm\bar{3}n$	6.900	6.900	11.100	[20]

reproduce overall features of the phase diagram and thermodynamic properties. The thermodynamic parameters of the Ag–Sn system reported by OH et al [28] are accepted in the present work and the calculated phase diagram of the Ag–Sn system is shown in Fig. 1(a).

2.2 Ag−Zr binary system

The Ag−Zr binary phase diagram was experimentally determined [29−33]. RAUB and ENGEL [29] and BETTERTON et al [31] clearly revealed two intermediate phases, i.e., AgZr and $AgZr_2$, by using differential thermal analysis (DTA), XRD and optical microscopy methods. MASSALSKI et al [34], KARAKAYA and THOMPSON [17] critically evaluated the constitution, crystallography and thermodynamic data of the Ag−Zr system based on Refs. [29−33] and constructed the phase diagram of the Ag−Zr system. HE et al [35] optimized the Ag–Zr system by using the CALPHAD method; however, the thermodynamic model parameters can induce an inverse liquid miscibility gap in the Ag−Zr system at high temperature. KANG and JUNG [18] used modified quasichemical model to assess the system. Though the calculated phase diagram of the Ag−Zr system is consistent with the experimental data [29−33], the quasichemical model can be only applied in Factsage software and it is not compatible with Pandat and Thermo-calc softwares. Then, HSIAO et al [36] updated the thermodynamic description of the Ag−Zr system and obtained a set of thermodynamic parameters, which can reproduce the measured phase diagram and thermodynamic data well. Thus, the thermodynamic parameters from HSIAO et al [36] are adopted in the present work and the calculated Ag−Zr phase diagram is shown in Fig. 1(b).

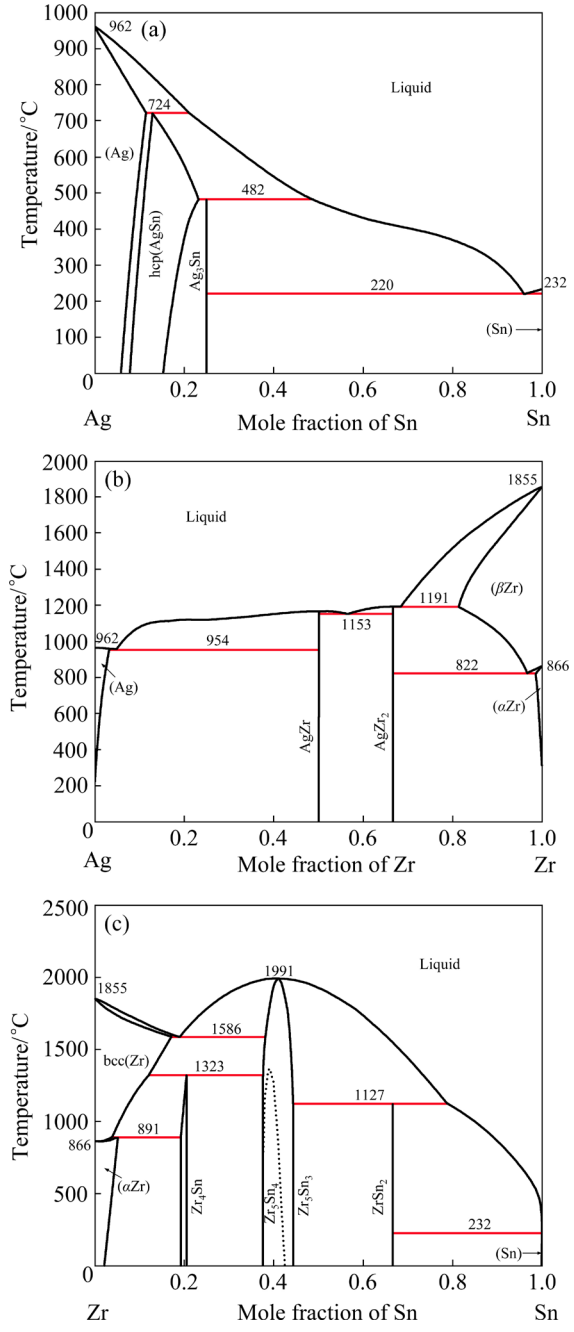

Fig. 1 Calculated Ag−Sn (a), Ag−Zr (b) and Zr−Sn (c) phase diagrams using thermodynamic parameters from OH et al [28], HSIAO et al [36] and PÉREZ et al [46], respectively

2.3 Sn−Zr binary system

The phase equilibria and thermodynamic properties of the Sn−Zr system have been investigated [37−45]. MCPHERSON and HANSEN [37] first constructed the phase diagram of Sn–Zr system by XRD and micrographic analysis and then it was updated by different authors [38−45]. It contains three intermediate phases, i.e., $ZrSn_2$, Zr_5Sn_3 and Zr_4Sn. The earlier controversies mainly concentrated on the structure of the Zr_4Sn phase and the phase boundary of (αZr) and Zr_4Sn. GRAN et al [39] found that the Zr_4Sn phase was energetically favored with the structure prototype of Cr_3Si and the deviation from the stoichiometric ratio of 3/1 was attributed to the substitution of Zr on the Sn sites. MASCLET et al [44] revised the phase boundary by discrete Fourier transform calculations method and found that the solubility of Sn in the (αZr) phase decreased as the temperature decreased, from 6 at.% at 900 °C to 4 at.% at 600 °C. The recent controversies focused on the

configurations and thermodynamic stabilities of the Zr_5Sn_4 phase in the range of 37.5−44.4 at.% Sn. BAYKOV et al [45] theoretically predicted Zr_5Sn_4 as stable phase due to the hybridization of Sn 5p with Zr 4d electronic states. PÉREZ et al [46] confirmed the structural correlation between them and observed the existence of a miscibility gap by metallurgical characterization. Thus, the Zr_5Sn_{3+x} phase was employed in the thermodynamic modeling of the Sn−Zr system from PÉREZ et al [46]. The thermodynamic parameters of the Sn−Zr system from PÉREZ et al [46] are adopted in the present work and the calculated Sn–Zr phase diagram is shown in Fig. 1(c).

2.4 Ag−Sn−Zr ternary system

So far, no phase equilibria and thermodynamic properties of the Ag−Sn−Zr ternary system were reported in the literature. As a part of our efforts to establish a thermodynamic database for multi-component Ag-based and Zr-based alloys [47−49], the present work is dedicated to determine the isothermal sections of the Ag−Sn−Zr system at 500, 700 and 900 °C, study the solidification microstructure of some representative as-cast alloys and obtain a set of reliable thermodynamic parameters of the Ag−Sn−Zr system.

3 Experimental

In order to determine the phase equilibria of the Ag−Sn−Zr system at 500, 700 and 900 °C, twenty-two ternary equilibrated alloys and eight as-cast alloys were prepared by melting mixture of the high purity Ag (99.99 wt.%) rods, Sn (99.99 wt.%) blocks and Zr (99.99 wt.%) blocks (China New Metal Materials Technology Co., Ltd.) as starting materials. The equilibrated alloys and as-cast alloys, each with a mass of approximately 1 g, were prepared in a non-consumable vacuum arc-melting furnace (WK-I, Physcience Opto-electronics Co., Ltd., Beijing, China) with water-cooled copper crucible in 99.999 % pure Ar (Shanghai Pressure Reducer Factory Co., Ltd.) atmosphere. The experimental pressure (p) of the protective gas is 0.98 MPa (standard uncertainty (u): $u(p)$=0.5%). In order to reduce the oxygen pollution of the sample during smelting process, the deoxidant (typically zirconium) was first melted, which could reduce the oxygen amount in the melting vessel. Each alloy was re-melted at least five times to make sure its homogeneity. The alloys after arc melting were not subjected to chemical analysis since the mass losses were less than 1 wt.% for all alloys. Then, the equilibrated alloys were wrapped with molybdenum wire, sealed in evacuated quartz capsules with vacuum sealing machine (MRVS-1002, Wuhan Bailibo Technology Co., Ltd., China), and annealed at 500 °C (50 d), 700 °C (30 d) and 900 °C (15 d) in the high-temperature diffusion furnace (KSL−1200X, Hefei Kejing Material Technology Co., Ltd., China), followed by quenching in cold water. The as-cast alloys were cut into two pieces for XRD and SEM/EDS measurements after arc melting and cooling naturally to room temperature in Ar gas atmosphere with the pressure of 0.9 MPa ($u(p)$=0.5%).

The powder XRD measurements of the annealed alloys and the as-cast alloys were performed using a Cu K_α radiation at 40 kV and 300 mA (Smartlab SE, Rigaku corporation, Japan) at room temperature. Diffraction patterns were generally acquired in a scan step 0.02° of over a 2θ range of 20°−80°. Then, these samples were further examined using scanning electron microscopy equipped with energy dispersive X-ray analysis (SEM/EDS) (acceleration voltage of 20 kV, scanning speed of 10 μs, working distance of 4.5 mm) (JSM−6360LV/GENESIS2000XM60, JEOL, Japan). The equipment standard uncertainty is 0.05 at.%. Generally, three points of each phase were measured by EDS analysis and their average value was taken as the phase composition. The phases and compositions of the annealed alloys are listed in Table S1 in Supplementary materials in detail. The phase composition wasn't calibrated to the standard sample and the error range of the average value compared to the compositions of each points was about 1 at.%.

4 Thermodynamic model

The Gibbs energy functions of the pure elements Ag, Sn and Zr are taken from the SGTE database compiled by DINSDALE [27]. The thermodynamic parameters of the Ag−Sn, Ag−Zr and Sn−Zr binary systems reported by OH et al [28], HSIAO et al [36] and PÉREZ et al [46] are accepted in the present work.

The phases in the Ag−Sn−Zr system to be optimized in the present work are as follows: solution phases, i.e., liquid, (Ag), (βSn), (αZr), (βZr) and hcp(AgSn); six binary phases extending into the ternary system, i.e., Ag_3Sn, AgZr, $AgZr_2$, $ZrSn_2$, Zr_5Sn_3 and Zr_4Sn.

4.1 Solution phases

The solution phases are described by the substitutional solution model. The molar Gibbs energy of solution phase φ is expressed by the Redlich−Kister−Muggianu polynomial [50]:

$$\begin{aligned} G^{\varphi} = {} & x_{\mathrm{Ag}} \cdot {}^{\mathrm{o}}G^{\varphi}_{\mathrm{Ag}} + x_{\mathrm{Sn}} \cdot {}^{\mathrm{o}}G^{\varphi}_{\mathrm{Sn}} + x_{\mathrm{Zr}} \cdot {}^{\mathrm{o}}G^{\varphi}_{\mathrm{Zr}} + \\ & RT(x_{\mathrm{Ag}} \cdot \ln x_{\mathrm{Ag}} + x_{\mathrm{Sn}} \cdot \ln x_{\mathrm{Sn}} + x_{\mathrm{Zr}} \cdot \ln x_{\mathrm{Zr}}) + \\ & x_{\mathrm{Ag}} \cdot x_{\mathrm{Sn}} \cdot L^{\varphi}_{\mathrm{Ag,Sn}} + x_{\mathrm{Sn}} \cdot x_{\mathrm{Zr}} \cdot L^{\varphi}_{\mathrm{Sn,Zr}} + \\ & x_{\mathrm{Ag}} \cdot x_{\mathrm{Zr}} \cdot L^{\varphi}_{\mathrm{Ag,Zr}} + x_{\mathrm{Ag}} \cdot x_{\mathrm{Sn}} \cdot x_{\mathrm{Zr}} \cdot (x_{\mathrm{Ag}} \cdot {}^{0}L^{\varphi}_{\mathrm{Ag,Sn,Zr}} + \\ & x_{\mathrm{Sn}} \cdot {}^{1}L^{\varphi}_{\mathrm{Ag,Sn,Zr}} + x_{\mathrm{Zr}} \cdot {}^{2}L^{\varphi}_{\mathrm{Ag,Sn,Zr}}) \end{aligned} \quad (1)$$

where ${}^{\mathrm{o}}G^{\varphi}_{i}$ stands for the Gibbs free energy of the pure component i (i=Ag, Sn or Zr) in the reference state for φ phase, R represents the molar gas constant, T is the thermodynamic temperature, and x_{Ag}, x_{Sn} and x_{Zr} are the molar fractions of the elements Ag, Sn and Zr, respectively. The ternary interaction parameters, ${}^{0}L^{\varphi}_{\mathrm{Ag,Sn,Zr}}$, ${}^{1}L^{\varphi}_{\mathrm{Ag,Sn,Zr}}$ and ${}^{2}L^{\varphi}_{\mathrm{Ag,Sn,Zr}}$ are linearly temperature-dependent, which can be expressed as $L^{\varphi}_{\mathrm{Ag,Sn,Zr}} = A + B \cdot T$. The coefficients A and B will be optimized according to the experimental data obtained from the present work and the literature.

4.2 Binary phases extending into ternary system

According to the experimental data, the binary phases Ag_3Sn in the Ag−Sn system, AgZr, $AgZr_2$ in the Ag−Zr system and $ZrSn_2$, Zr_5Sn_3 and Zr_4Sn in the Zr−Sn system exhibit some solubilities for Zr, Sn and Ag, respectively. Sublattice models [51,52] are used to describe these binary phases. From the experimental results, it is assumed that Ag and Sn substitute each other in the sublattice models. Thus, in the present work, the Ag_3Sn, AgZr, $AgZr_2$, $ZrSn_2$, Zr_5Sn_3 and Zr_4Sn phases are modeled as $(\mathbf{Ag})_3(\mathrm{Ag},\mathbf{Sn})_1$, $(\mathbf{Ag},\mathrm{Sn})_1(\mathbf{Zr})_1$, $(\mathbf{Ag},\mathrm{Sn})_1(\mathbf{Zr})_2$, $(\mathbf{Zr})_1(\mathrm{Ag},\mathbf{Sn})_2$, $(\mathbf{Zr})_5(\mathrm{Ag},\mathbf{Sn})_3(\mathrm{Ag},\mathrm{Sn},\mathbf{Va})_1$ and $(\mathrm{Ag},\mathrm{Sn},\mathbf{Zr})_3(\mathrm{Ag},\mathbf{Sn},\mathrm{Zn})_1$, respectively. In these sublattices, the boldfaces mean the normal atoms (i.e., major species). Taking the $AgZr_2$ phase as an example, its Gibbs energy can be expressed as follows:

$$\begin{aligned} G^{\mathrm{AgZr_2}} = {} & y'_{\mathrm{Ag}} \cdot {}^{\mathrm{o}}G^{\mathrm{AgZr_2}}_{\mathrm{Ag:Zr}} + y'_{\mathrm{Sn}} \cdot {}^{\mathrm{o}}G^{\mathrm{AgZr_2}}_{\mathrm{Sn:Zr}} + \\ & RT\left(y'_{\mathrm{Ag}} \cdot \ln y'_{\mathrm{Ag}} + y'_{\mathrm{Sn}} \cdot \ln y'_{\mathrm{Sn}}\right) + \\ & y'_{\mathrm{Ag}} y'_{\mathrm{Sn}} \left[{}^{0}L^{\mathrm{AgZr_2}}_{\mathrm{Ag,Sn:Zr}} + (y'_{\mathrm{Ag}} - y'_{\mathrm{Sn}})^{1} \cdot {}^{1}L^{\mathrm{AgZr_2}}_{\mathrm{Ag,Sn:Zr}} + \cdots\right] \end{aligned} \quad (2)$$

where y'_{Ag} and y'_{Sn} represent the site fractions of Ag and Sn in the first sublattice, respectively. ${}^{\mathrm{o}}G^{\mathrm{AgZr_2}}_{\mathrm{Ag:Zr}}$ and ${}^{\mathrm{o}}G^{\mathrm{AgZr_2}}_{\mathrm{Sn:Zr}}$ are the Gibbs free energies of end-members of the $AgZr_2$ phase. The interaction parameters ${}^{0}L^{\mathrm{AgZr_2}}_{\mathrm{Ag,Sn:Zr}}$ and ${}^{1}L^{\mathrm{AgZr_2}}_{\mathrm{Ag,Sn:Zr}}$ are also linearly temperature-dependent, which can be expressed as $L^{\mathrm{AgZr_2}}_{\mathrm{Ag,Sn:Zr}} = a + b \cdot T$, and the coefficients a and b are optimized in the present work based on the experimental data. Analogous expressions similar to Eq. (2) are applied to describing the Gibbs energies of the Ag_3Sn, AgZr, $ZrSn_2$, Zr_5Sn_3 and Zr_4Sn phases.

5 Results and discussion

Twenty-two ternary alloys were prepared to determine the phase equilibria of the Ag−Sn−Zr system at 500, 700 and 900 °C, and eight as-cast alloys were prepared to study the solidification behavior of the alloys, respectively. The phases with lattice parameters identified by XRD and the compositions and microstructures measured by SEM/EDS of the samples are listed in Table S1 in Supplementary material for detail.

5.1 Microstructures of equilibrated alloys

Figure 2 presents the backscattered electron (BSE) images and the XRD patterns of the representative ternary alloys, A1 ($Ag_{19}Sn_{46}Zr_{35}$), A4 ($Ag_{55}Sn_{10}Zr_{35}$) and A6 ($Ag_{30}Sn_5Zr_{65}$) annealed at 500 °C for 50 d, respectively. The composition of each alloy was examined by EDS after annealing and the standard X-ray diffraction patterns for individual phases are displayed. Figures 2(a, b) show the BSE micrograph and XRD diffraction patterns of Alloy A1, respectively. The microstructural analysis results of the equilibrated alloy, A1, clearly show three distinct phases, i.e., the white, gray and dark phases, which correspond to hcp(AgSn), $ZrSn_2$ and Zr_5Sn_3, respectively. This is confirmed by XRD analysis and the characteristic peaks of the three phases are distinctly described by the corresponding standard spectral lines. Therefore,

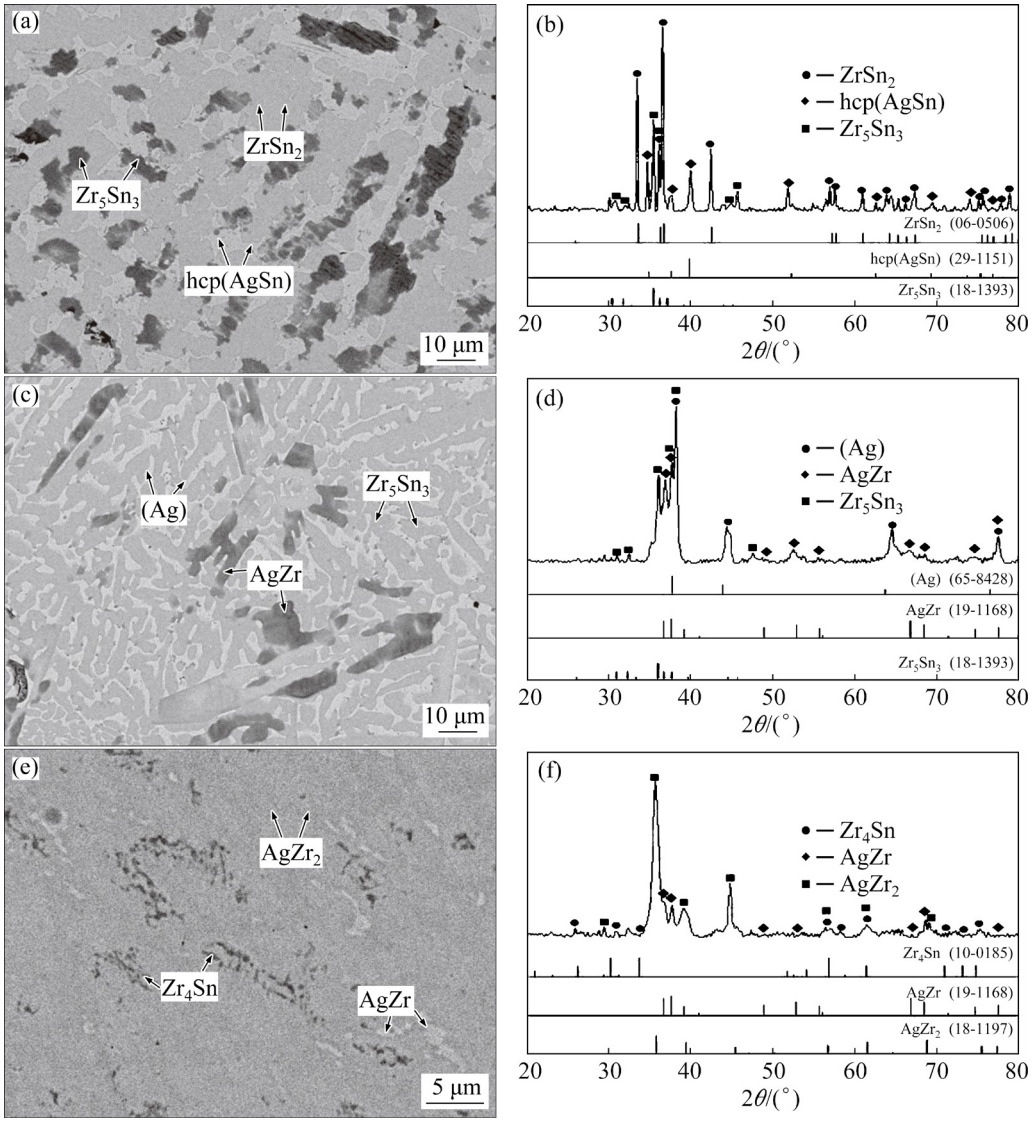

Fig. 2 BSE micrographs (a, c, e) and XRD patterns (b, d, f) of Ag−Sn−Zr alloys annealed at 500 °C for 50 d: (a, b) Alloy A1 ($Ag_{19}Sn_{46}Zr_{35}$); (c, d) Alloy A4 ($Ag_{55}Sn_{10}Zr_{35}$); (e, f) Alloy A6 ($Ag_{30}Sn_5Zr_{65}$)

it can be concluded that Alloy A1 is located in the three-phase region hcp(AgSn) + $ZrSn_2$ + Zr_5Sn_3. The measured solubilities of Zr in the hcp(AgSn) phase and Ag in the $ZrSn_2$ and Zr_5Sn_3 phases are about 1.77, 0.41 and 1.09 at.%, respectively. In Alloy A4, a three- phase equilibrium constituted by bright (Ag), light gray Zr_5Sn_3 and dark gray AgZr is identified, as shown in Fig. 2(c). The characteristic peaks of the three phases are distinctly described by the corresponding standard spectral lines shown in Fig. 2(d). Thus, Alloy A4 is located in the three-phase region, i.e., (Ag) + Zr_5Sn_3 + AgZr. The measured solubility of Ag in the Zr_5Sn_3 phase is about 0.46 at.% and that of Sn in the AgZr phase is about 1.31 at.%. Figure 2(e) shows the BSE micrograph of Alloy A6, where a three-phase equilibrium, AgZr + $AgZr_2$ + Zr_4Sn, is identified. According to Fig. 2(e), the white phase is AgZr, the gray phase is $AgZr_2$, and the dark phase is Zr_4Sn. The corresponding XRD diffraction pattern of Alloy A6 shown in Fig. 2(f) illustrates that the characteristic peaks of the AgZr, $AgZr_2$ and Zr_4Sn phases are well distinguished. Combined with the BSE and XRD results, Alloy A6 is located in the three-phase region, i.e., AgZr + $AgZr_2$ + Zr_4Sn. The measured solubilities of Sn in the AgZr and $AgZr_2$ phases are about 2.57 and 1.84 at.%, respectively, and the solubility of Ag in the Zr_4Sn phase is about 2.65 at.%, respectively.

Similarly, the phases and compositions of Alloys A2 ($Ag_{74}Sn_{16}Zr_{10}$), A3 ($Ag_{20}Sn_{32}Zr_{48}$), A5 ($Ag_{10}Sn_{23}Zr_{67}$) and A7 ($Ag_7Sn_{10}Zr_{83}$) were also

analyzed and listed in Table S1 in Supplementary materials in detail. Alloy A5 is located in the three-phase region Zr_5Sn_3 + AgZr + Zr_4Sn. Alloys A2, A3 and A7 are located in the two-phase regions hcp(AgSn) + Zr_5Sn_3, Zr_5Sn_3 + Zr_5Sn_4 and Zr_4Sn + (αZr), respectively.

Figure 3 shows the BSE images and XRD patterns of the representative ternary alloys, B4 ($Ag_{55}Sn_{10}Zr_{35}$), B6 ($Ag_{30}Sn_5Zr_{65}$) and B7 ($Ag_8Sn_{10}Zr_{82}$), annealed at 700 °C for 30 d. Figures 3(a, b) show the BSE micrograph and XRD patterns for Alloy B4, respectively. As shown in Fig. 3(a), three phases, i.e., (Ag), Zr_5Sn_3 and AgZr can be observed. The white phase is (Ag), the gray phase is Zr_5Sn_3 and the dark phase is AgZr. The XRD pattern shown in Fig. 3(b) illustrates that the characteristic peaks of the (Ag), Zr_5Sn_3 and AgZr phases are well distinguished. Therefore, Alloy B4 is confirmed to be located in the three-phase region (Ag) + Zr_5Sn_3 + AgZr. The measured solubility of Sn in the AgZr phase is about 0.37 at.% and that of Ag in the Zr_5Sn_3 phase is about 0.86 at.%. Figures 3(c, d) show the BSE micrograph and XRD patterns of Alloy B6, respectively. The XRD pattern indicates that Alloy B6 contains three phases, i.e., AgZr, $AgZr_2$ and Zr_4Sn, which correspond to the bright, gray and dark regions of the BSE micrograph shown in Fig. 3(c). Thus, Alloy B6 is located in the three-phase region, i.e., AgZr + $AgZr_2$ + Zr_4Sn. The measured solubilities of Sn in the AgZr and $AgZr_2$ phases are about 2.46 and 2.24 at.% and the measured solubility of Ag in the Zr_4Sn phase is about 2.18 at.%. The microstructural analysis results of the equilibrated

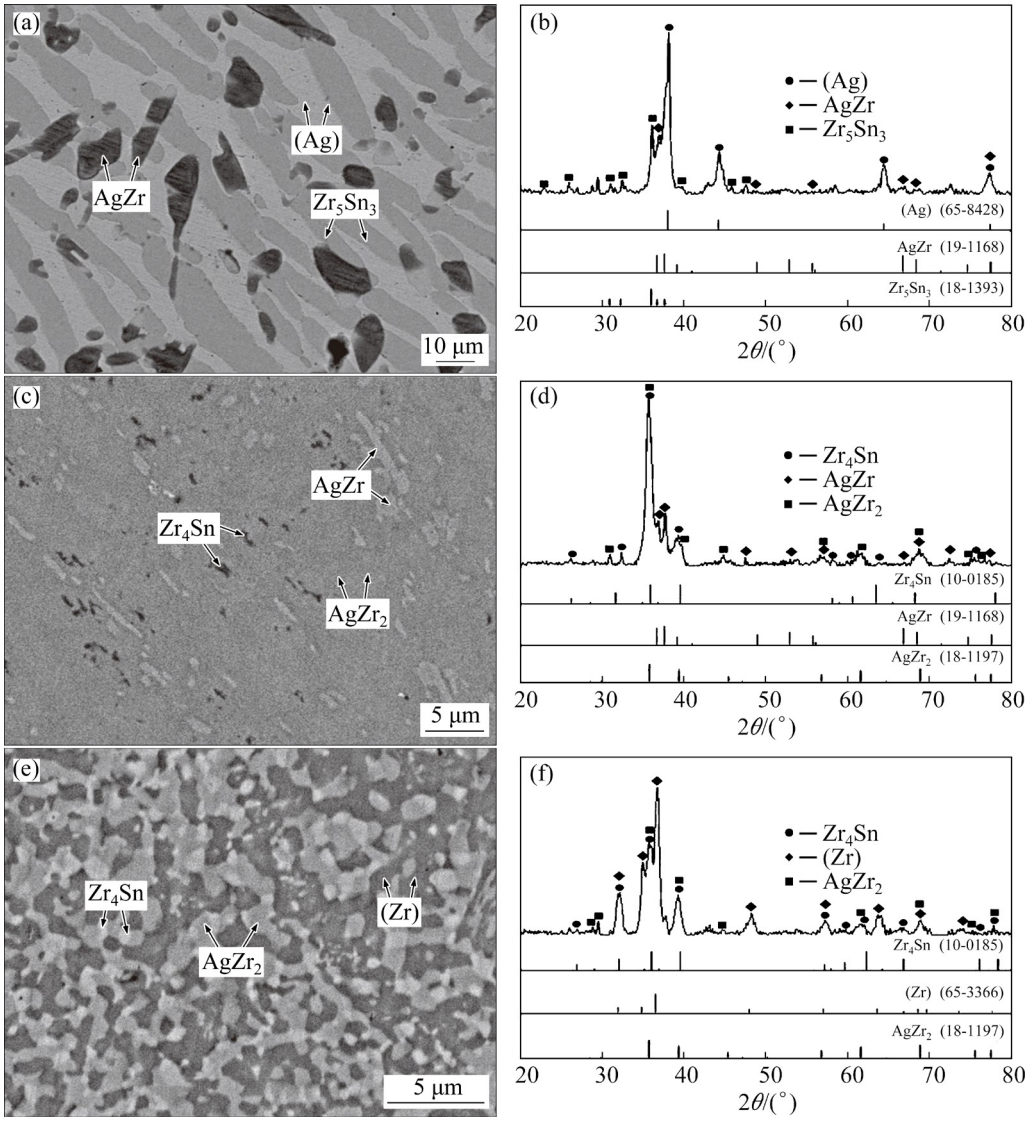

Fig. 3 BSE micrographs (a, c, e) and XRD patterns (b, d, f) of Ag–Sn–Zr alloys annealed at 700 °C for 30 d: (a, b) Alloy B4 ($Ag_{55}Sn_{10}Zr_{35}$); (c, d) Alloy B6 ($Ag_{30}Sn_5Zr_{65}$); (e, f) Alloy B7 ($Ag_8Sn_{10}Zr_{82}$)

Alloy B7, presented in Fig. 3(e) clearly show three distinct phases, i.e., the white, gray and dark phases, which correspond to Zr_4Sn, $AgZr_2$ and (αZr), respectively. This is confirmed by XRD pattern shown in Fig. 3(f). Therefore, it can be concluded that Alloy B7 is located in the Zr_4Sn + $AgZr_2$ + (αZr) three-phase region. The measured solubilities of Ag in the Zr_4Sn and (αZr) phases and Sn in the $AgZr_2$ phase are about 0.46, 0.76 and 2.54 at.%, respectively.

The phases and compositions of Alloys B1 ($Ag_{68}Sn_{22}Zr_{10}$), B2 ($Ag_{74}Sn_{17}Zr_9$), B3 ($Ag_{20}Sn_{32}Zr_{48}$) and B5 ($Ag_{20}Sn_{17}Zr_{63}$) were also analyzed and listed in Table S1 in Supplementary materials in detail. Alloys B3 and B5 are located in the three-phase region (Ag) + Zr_5Sn_3 + Zr_5Sn_4 and Zr_5Sn_3 + AgZr + Zr_4Sn, respectively. Alloys B1and B2 are located in the two-phase region hcp(AgSn) + Zr_5Sn_3.

Figure 4 shows the BSE images and XRD patterns of the representative ternary alloys, C3 ($Ag_{70}Sn_5Zr_{25}$), C6 ($Ag_{33}Sn_3Zr_{64}$) and C7 ($Ag_{20}Sn_{10}Zr_{70}$), annealed at 900 ℃ for 15 d. The microstructural analysis results of the equilibrated alloy, C3, presented in Fig. 4(a) clearly show three distinct phases, i.e., white, gray and dark phases, which correspond to (Ag), AgZr and Zr_5Sn_3, respectively. This is confirmed by XRD analysis shown in Fig. 4(b). Therefore, it can be concluded that Alloy C3 is located in (Ag) + AgZr + Zr_5Sn_3 three-phase region. The measured solubilities of Ag in the Zr_5Sn_3 phase and Sn in the AgZr and (Ag) phases are about 1.87, 0.77 and 1.77 at.%, respectively. Figure 4(c) shows the microstructure of Alloy C6, in which a three-phase equilibrium,

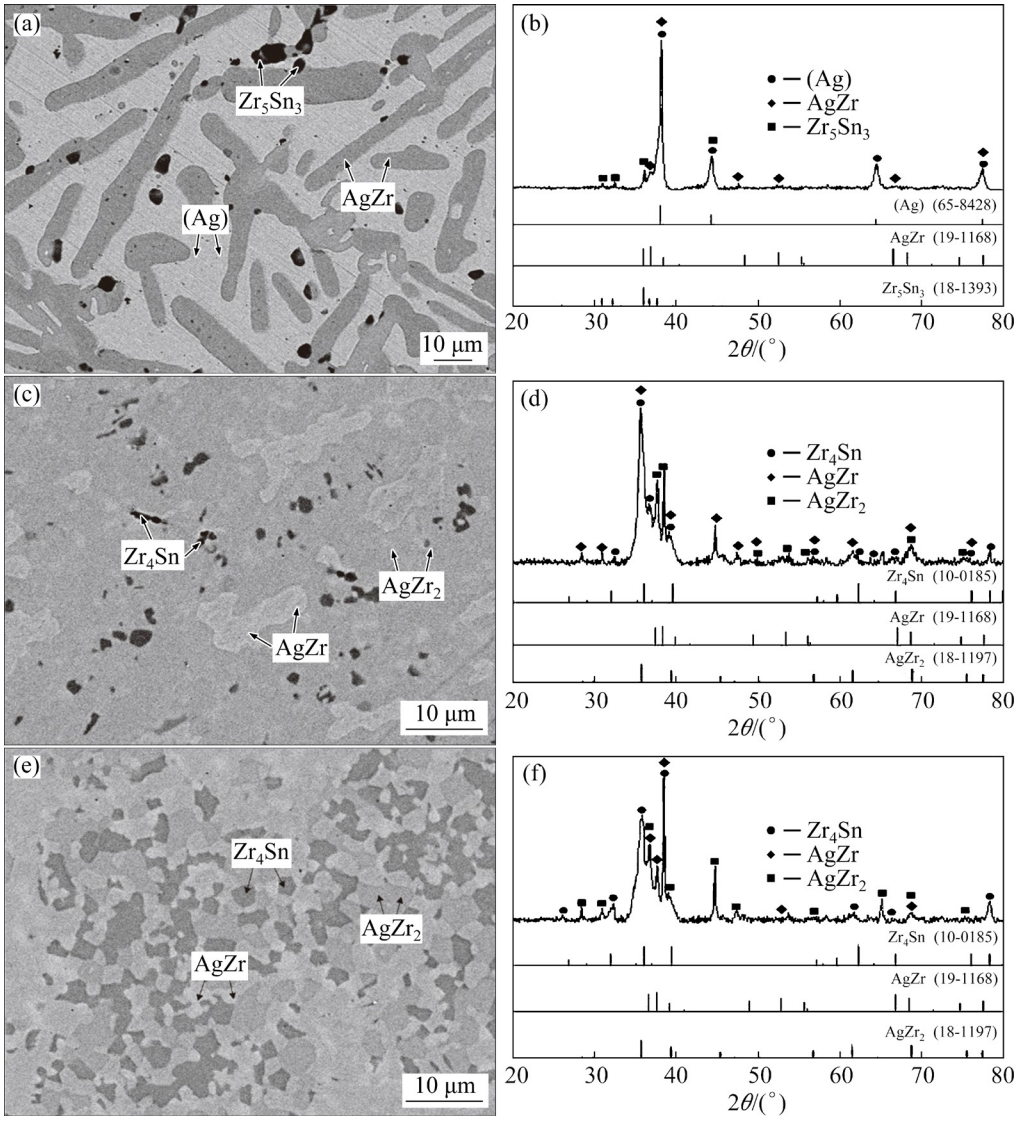

Fig. 4 BSE micrographs (a, c, e) and XRD patterns (b, d, f) of Ag−Sn−Zr alloys annealed at 900 ℃ for 15 d: (a, b) Alloy C3 ($Ag_{70}Sn_5Zr_{25}$); (c, d) Alloy C6 ($Ag_{33}Sn_3Zr_{64}$); (e, f) Alloy C7 ($Ag_{20}Sn_{10}Zr_{70}$)

AgZr + $AgZr_2$ + Zr_4Sn, is identified. The XRD pattern shown in Fig. 4(d) indicates that Alloy C6 contains three phase, i.e., AgZr, $AgZr_2$ and Zr_4Sn, which correspond to the bright, gray and dark regions, respectively. Therefore, Alloy C6 is located in the three-phase region, i.e., AgZr + $AgZr_2$ + Zr_4Sn. The measured solubilities of Sn in the AgZr and $AgZr_2$ phases are 1.64 and 1.53 at.%, respectively. The BSE micrograph of Alloy C7 is shown in Fig. 4(e) and three phases, i.e., AgZr, $AgZr_2$ and Zr_4Sn, can be observed. The white phase is AgZr, the gray phase is $AgZr_2$ and the dark phase is Zr_4Sn. The XRD pattern of Alloy C7 shown in Fig. 4(f) illustrates that the characteristic peaks of the AgZr, $AgZr_2$ and Zr_4Sn phases are well distinguished. Combined with the BSE and XRD results, Alloy C7 is located in the three-phase region, i.e., AgZr + $AgZr_2$ + Zr_4Sn. The measured solubilities of Sn in the AgZr and $AgZr_2$ phases are about 2.09 and 2.15 at.%, respectively, and the solubility of Ag in the Zr_4Sn phase is about 1.49 at.%.

The phases and compositions of Alloys C1 ($Ag_{21}Sn_{34}Zr_{45}$), C2 ($Ag_{20}Sn_{30}Zr_{50}$), C4 ($Ag_{37}Sn_{18}Zr_{45}$), C5 ($Ag_{20}Sn_{17}Zr_{63}$) and C8 ($Ag_{12}Sn_8Zr_{80}$) were also analyzed and listed in Table S1 in Supplementary materials in detail. Alloys C2, C4, C5 and C8 are located in the three-phase regions, i.e., (Ag) + Zr_5Sn_3 + Zr_5Sn_4, (Ag) + Zr_5Sn_3 + AgZr, Zr_5Sn_3 + AgZr + Zr_4Sn and Zr_4Sn + $AgZr_2$ + (βZr), respectively. Alloys C1 is located in the two-phase region (Ag) + Zr_5Sn_3.

5.2 Isothermal sections at 500, 700 and 900 °C

Based on the experimental analysis above, the phase equilibria of the Ag–Sn–Zr system at 500, 700 and 900 °C were obtained in the present work. For the isothermal section at 500 °C, four three-phase regions, i.e., hcp(AgSn) + $ZrSn_2$ + Zr_5Sn_3, (Ag) + Zr_5Sn_3 + AgZr, Zr_5Sn_3 + AgZr + Zr_4Sn and AgZr + Zr_4Sn + $AgZr_2$, and three two-phase regions, i.e., hcp(AgSn) + Zr_5Sn_3, Zr_5Sn_3 + Zr_5Sn_4 and Zr_4Sn + (αZr) were determined. According to the phase regions of Alloys A2, A3 and A4 and the Gibbs phase rule, two three-phase regions hcp(AgSn) + Zr_5Sn_3 + (Ag) and Zr_5Sn_3 + Zr_5Sn_4 + (Ag) were extrapolated. Similarly, a three-phase region, i.e., Zr_4Sn + $AgZr_2$ + (αZr), could be extrapolated according to the experimental results of Alloys A6 and A7 in view of the Gibbs phase rule. The measured average solubilities of Ag in the $ZrSn_2$, Zr_5Sn_3, Zr_5Sn_4 and Zr_4Sn phases are about 0.41, 1.07, 0.58 and 1.86 at.%, respectively. The measured average solubilities of Sn in the AgZr and $AgZr_2$ phases and Zr in the hcp(AgSn) phase are about 1.74, 1.84 and 1.81 at.%, respectively. It can be noted that the solubilities of the third element in binary compounds in the Ag−Sn, Ag−Zr and Sn−Zr systems at 500 °C are less than 2 at.%.

For the isothermal section at 700 °C, five three-phase regions, i.e., (Ag) + Zr_5Sn_3 + Zr_5Sn_4, (Ag) + Zr_5Sn_3 + AgZr, Zr_5Sn_3 + AgZr + Zr_4Sn, AgZr + $AgZr_2$ + Zr_4Sn and Zr_4Sn + $AgZr_2$ + (αZr) and one two-phase regions, i.e., hcp(AgSn) + Zr_5Sn_3 were determined. According to the experimental results of Alloys B2 and B3 and the Gibbs phase rule, a three-phase region hcp(AgSn) + Zr_5Sn_3 + (Ag) is extrapolated. Based on the phase equilibria of the Ag–Sn–Zr system at 500 °C and the Gibbs phase rule, Alloy B1 could be located in the three-phase region, i.e., hcp(AgSn) + Zr_5Sn_3 + $ZrSn_2$. The measured average solubilities of Ag in the Zr_5Sn_3, Zr_5Sn_4 and Zr_4Sn phases are about 1.69, 0.75 and 1.79 at.%, respectively. The measured average solubilities of Sn in the AgZr and $AgZr_2$ phases and Zr in the hcp(AgSn) phase are about 1.54, 2.39 and 1.41 at.%, respectively. It can be noted that the solubilities of the third element in binary compounds in the Ag−Sn, Ag−Zr and Sn−Zr systems at 700 °C are less than 3 at.%.

For the isothermal section at 900 °C, five three-phase regions, i.e., (Ag) + Zr_5Sn_3 + Zr_5Sn_4, (Ag) + Zr_5Sn_3 + AgZr, Zr_5Sn_3 + AgZr + Zr_4Sn, AgZr + Zr_4Sn + $AgZr_2$ and Zr_4Sn + $AgZr_2$ + (βZr) and one two-phase region, i.e., (Ag) + Zr_5Sn_3 were determined. According to the experimental results of Alloys C1 and C2 and the phase relationship of the Ag−Sn−Zr system at 500 and 700 °C applying the Gibbs phase rule, a three-phase region Liquid + (Ag) + Zr_5Sn_3 is extrapolated. The measured average solubilities of Ag in the Zr_5Sn_3, Zr_5Sn_4 and Zr_4Sn phases are about 0.89, 0.38 and 1.23 at.%, respectively. The measured average solubilities of Sn in the AgZr and $AgZr_2$ phases are about 1.47 and 1.41 at.%, respectively. It can be noted that the solubilities of the third element in binary compounds in the Ag−Sn, Ag−Zr and Sn−Zr systems at 900 °C are less than 2 at.%.

5.3 Thermodynamic calculation

Based on the experimental data obtained from the present work and literature, the thermodynamic parameters of the Ag–Sn–Zr system were evaluated by the optimization module PARROT [53] of the Thermo-Calc program, which works by minimizing the square sum of the differences between measured and calculated values. Step-by-step optimization procedures [54,55] were utilized in the present assessment.

The optimization starts with the isothermal section at 500 °C. Firstly, according to the phase equilibria and the solubilities of Ag, Sn and Zr in the binary phases in the Sn−Zr, Ag−Zr and Ag−Sn systems, respectively, the interaction parameters *a* for these phases in Eq. (2) were optimized. Then, the isothermal sections at 700 and 900 °C were considered one by one in the optimization process. Next, the ternary interaction parameter *A* for the phase hcp(AgSn) in Eq. (1) was obtained by fitting the experimental data of isothermal sections and invariant reactions. Finally, all the parameters were optimized simultaneously. The thermodynamic parameters obtained in the present work are listed in Table 2.

Table 2 Thermodynamic parameters of Ag−Sn−Zr system obtained in present work

Phase	Model	Thermodynamic parameter
hcp	$(Ag,Sn,Zr)_1Va_{0.5}$	${}^0L^{hcp}_{Ag,Sn,Zr:Va} = -742130$
Zr_5Sn_3	$(\mathbf{Zr})_5(Ag,\mathbf{Sn})_3$-$(Ag,Sn,\mathbf{Va})_1$	${}^oG^{Zr_5Sn_3}_{Zr:Ag:Ag} = 12013 + 5\,{}^oG^{hcp}_{Zr} + 4\,{}^oG^{fcc}_{Ag}$, ${}^oG^{Zr_5Sn_3}_{Zr:Ag:Va} = 24653 + 5\,{}^oG^{hcp}_{Zr} + 3\,{}^oG^{fcc}_{Ag}$
Zr_4Sn	$(Ag,Sn,\mathbf{Zr})_3$-$(Ag,\mathbf{Sn},\mathbf{Zr})_1$	${}^oG^{Zr_4Sn}_{Ag:Ag} = 12082 + 4\,{}^oG^{fcc}_{Ag}$
$AgZr_2$	$(\mathbf{Ag},Sn)_{33}(\mathbf{Zr})_{67}$	${}^oG^{AgZr_2}_{Sn:Zr} = -158793.09 + {}^oG^{bct}_{Sn} + 2\,{}^oG^{hcp}_{Zr}$

The Gibbs energies for the pure elements were taken from the compilation of DINSDALE [27]; The thermodynamic parameters for the Ag–Sn, Ag–Zr and Sn–Zr systems from OH et al [28], HSIAO et al [36] and PÉREZ et al [46], respectively, were adopted in the present work

The calculated isothermal sections of the Ag−Sn−Zr system at 500, 700 and 900 °C compared with the experimental phase equilibria data obtained in the present work are presented in Figs. 5(a−c), respectively. The calculated phase equilibria are consistent with the measured ones. As can be seen from Fig. 5, seven three-phase regions in the isothermal sections at 500 and 700 °C and six three-phase regions at 900 °C are calculated. The calculated solubilities of Ag in the Zr_5Sn_3, Zr_5Sn_4 and Zr_4Sn phases, Sn in the AgZr and $AgZr_2$ phases and Zr in the hcp(AgSn) phase are about 0.97, 0.46, 1.56, 1.55, 1.78 and 1.80 at.% at 500 °C, respectively. The calculated solubilities of Ag in Zr_5Sn_3, Zr_5Sn_4 and Zr_4Sn phases, Sn in the AgZr

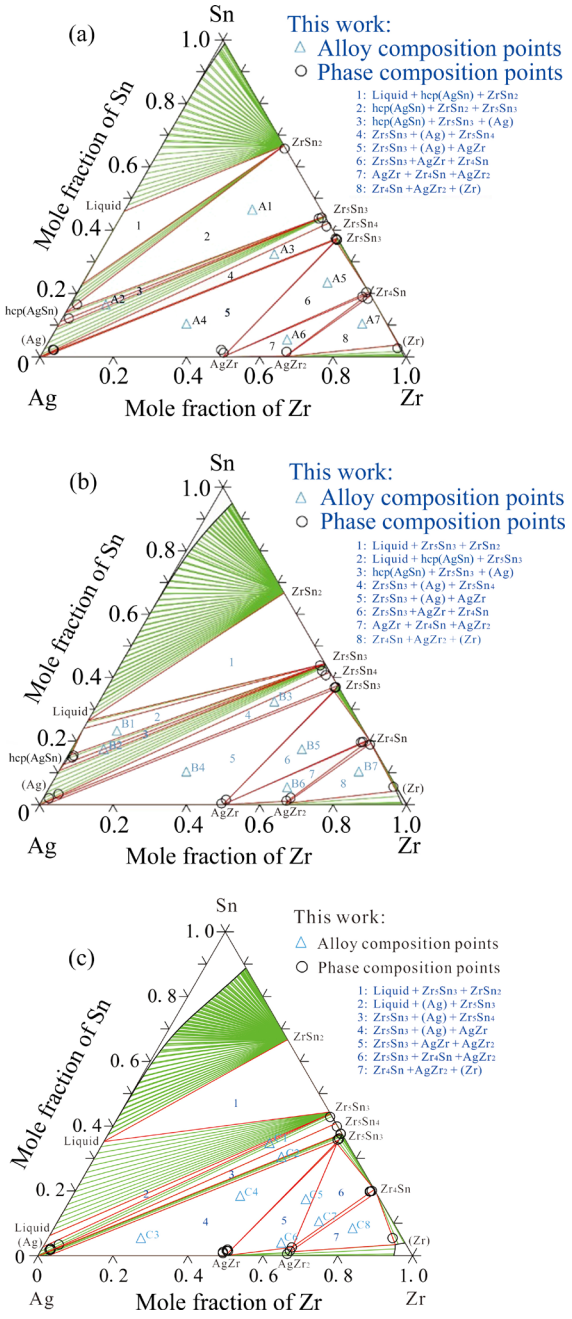

Fig. 5 Calculated isothermal sections of Ag–Sn–Zr system along with experimental data from the present work: (a) 500 °C; (b) 700 °C; (c) 900 °C

and $AgZr_2$ phases and Zr in the hcp(AgSn) phase are about 1.54, 0.69, 1.80, 1.32, 2.14 and 1.42 at.% at 700 °C, respectively. Similarly, the calculated solubilities of Ag in Zr_5Sn_3, Zr_5Sn_4 and Zr_4Sn phases and Sn in AgZr and $AgZr_2$ phases are about 0.88, 0.39, 1.35, 1.42 and 2.14 at.% at 900 °C, respectively. It can be concluded that the calculated solubilities of Ag, Sn and Zr in the binary phases in the Sn−Zr, Ag−Zr and Ag−Sn systems are consistent with the present experimental results.

The calculated liquidus projection of the Ag−Sn−Zr system according to the present thermodynamic parameters is presented in Fig. 6. The constructed reaction scheme of the Ag−Sn−Zr system according to the present calculations is presented in Fig. 7 to provide a better understanding of the solidification sequence and liquidus projection. It is worth noting that the calculated liquidus projection exists a large liquid phase separation region, i.e., liquid#1 + liquid#2. The predicted invariant reactions in the Ag−Sn−Zr system are listed in Table 3.

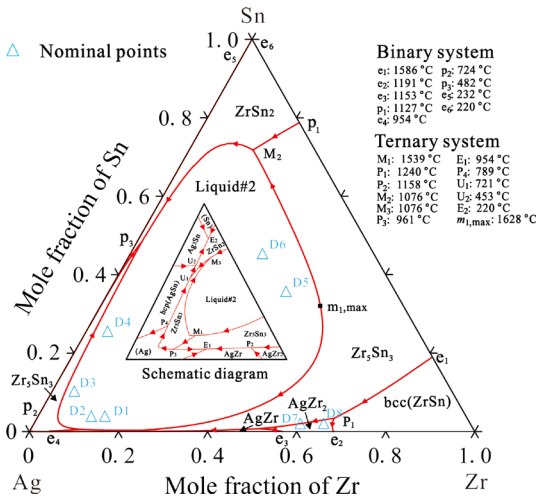

Fig. 6 Calculated liquidus projection of Ag–Sn–Zr system

5.4 Microstructure and solidification behavior of as-cast alloys

Regarding the condition of reactants and products, the phase transformation of an alloy system can be classified as liquid−solid, solid state and gas−solid reactions. Solidification is a process where the liquid phase gradually transforms into solid phases with temperature decreasing [56] and the Scheil module is employed to simulate the solidification process of as-cast Ag−Sn−Zr alloys under the non-equilibrium condition by using the present thermodynamic parameters. The final phase constitution and composition of the Ag−Sn−Zr alloys depend on the composition of alloys, the interface between the compound and the matrix, and the solid solubility of alloying elements. In order to provide more detail on the solidification behavior, eight Ag−Sn−Zr as-cast alloys were studied by SEM/EDS and Scheil module [57,58] was employed to simulate the solidification process of as-cast alloys by using the present thermodynamic parameters. The solidification phases and corresponding phase compositions of eight as-cast alloys determined by SEM/EDS are summarized in Table S2 in Supplementary material for detail. Figure 8 shows the microstructures of as-cast alloys, D1 ($Ag_{83}Sn_2Zr_{15}$), D5 ($Ag_{25}Sn_{35}Zr_{40}$), D6 ($Ag_{25}Sn_{45}Zr_{30}$) and D7 ($Ag_{39}Sn_1Zr_{60}$). Figure 9 shows the Gulliver−Scheil solidification curves of the as-cast alloys, D1−D8, which exhibit the solidification paths of these alloys. Figure 10 shows the calculated mole fraction of phases versus temperature for Alloys D1, D5, D6 and D7.

For the as-cast alloy, D1, its microstructure exists three different contrasts, as shown in Fig. 8(a, b). According to the EDS results, the bright, gray and dark fields are the (Ag), AgZr and Zr_5Sn_3 phases, respectively. No typically liquid-separated microstructures were observed. By combining Gulliver−Scheil solidification curve of Alloy D1 shown in Fig. 9(a), solidification path of Alloy D1 is as follows: Liquid → Liquid#1 + Liquid#2 + Zr_5Sn_3 → Liquid#1 + Zr_5Sn_3 → Liquid#1 + Zr_5Sn_3 + AgZr → Liquid#1 + Zr_5Sn_3 + AgZr + (Ag). The primary crystallization phase for Alloy D1 is Zr_5Sn_3. After the solidification of the primary phase of Zr_5Sn_3, Alloy D1 undergoes a peritectic reaction, i.e., Liquid + Zr_5Sn_3 → AgZr, then with the invariant reactions, i.e., Liquid → Zr_5Sn_3 + AgZr + (Ag), and ends with the eutectic microstructure (Zr_5Sn_3 + AgZr + (Ag)). These simulated results are in accordance with the microstructure observed in the present experiment (Figs. 8(a, b)). Figure 10(a) shows the mole fraction of phases in Alloy D1 as a function of temperature during the solidification process. It can be seen that the Zr_5Sn_3 phase precipitates from the liquid phase starting at 1575 °C, and then the AgZr and (Ag) phases precipitate successively at about 1097 and 954 °C, respectively. For mole fraction of

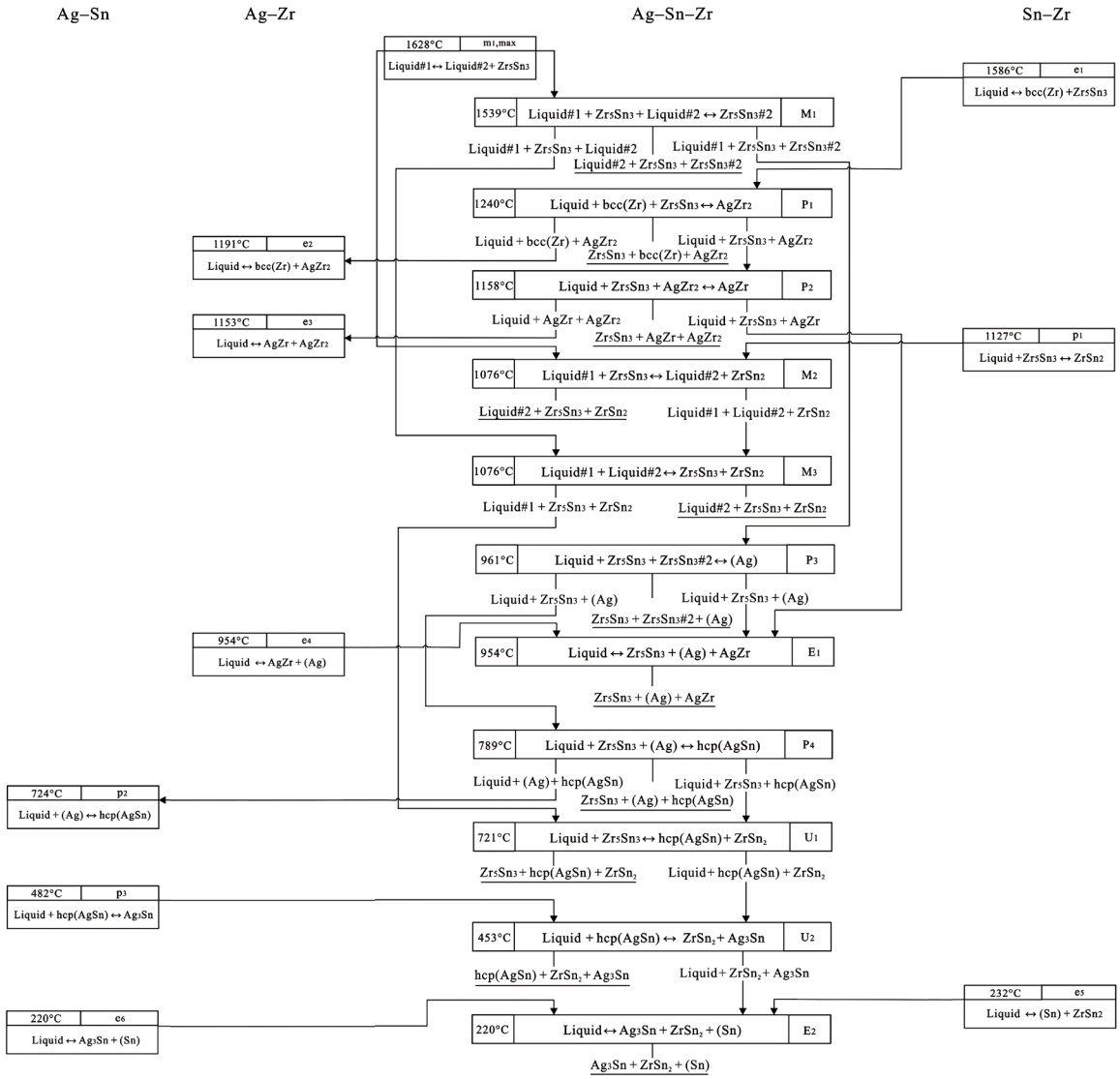

Fig. 7 Reaction scheme of Ag−Sn−Zr system associated with liquid phase

Table 3 Calculated invariant reactions in Ag–Sn–Zr system

Type	Invariant reaction	Temperature/°C	Composition/at.%		
			Ag	Sn	Zr
M1	Liquid#1 + Zr_5Sn_3 ⇌ Liquid#2 + Zr_5Sn_3#2	1539	72.69	7.59	19.72
P1	Liquid + (βZr) + Zr_5Sn_3 ⇌ $AgZr_2$	1240	29.87	3.41	66.72
P2	Liquid + Zr_5Sn_3 + $AgZr_2$ ⇌ AgZr	1158	48.11	0.75	51.15
M2	Liquid#1 + Zr_5Sn_3 ⇌ Liquid#2 + $ZrSn_2$	1076	13.90	71.76	14.33
M3	Liquid#1 + Liquid#2 ⇌ Zr_5Sn_3 + $ZrSn_2$	1076	68.87	6.72	24.41
P3	Liquid#1 + Zr_5Sn_3#1 + Zr_5Sn_3#2 ⇌ (Ag)	961	99.53	0.03	0.44
E1	Liquid ⇌ Zr_5Sn_3 + (Ag) + AgZr	954	95.10	0.01	4.89
P4	Liquid + Zr_5Sn_3 + (Ag) ⇌ hcp(AgSn)	789	84.41	15.58	0.01
U1	Liquid + Zr_5Sn_3 ⇌ hcp(AgSn) + $ZrSn_2$	721	72.78	27.21	0.01
U2	Liquid + hcp(AgSn) ⇌ $ZrSn_2$ + Ag_3Sn	453	45.66	54.32	0.01
E2	Liquid ⇌ Ag_3Sn + $ZrSn_2$ + (Sn)	220	4.09	95.90	0.01

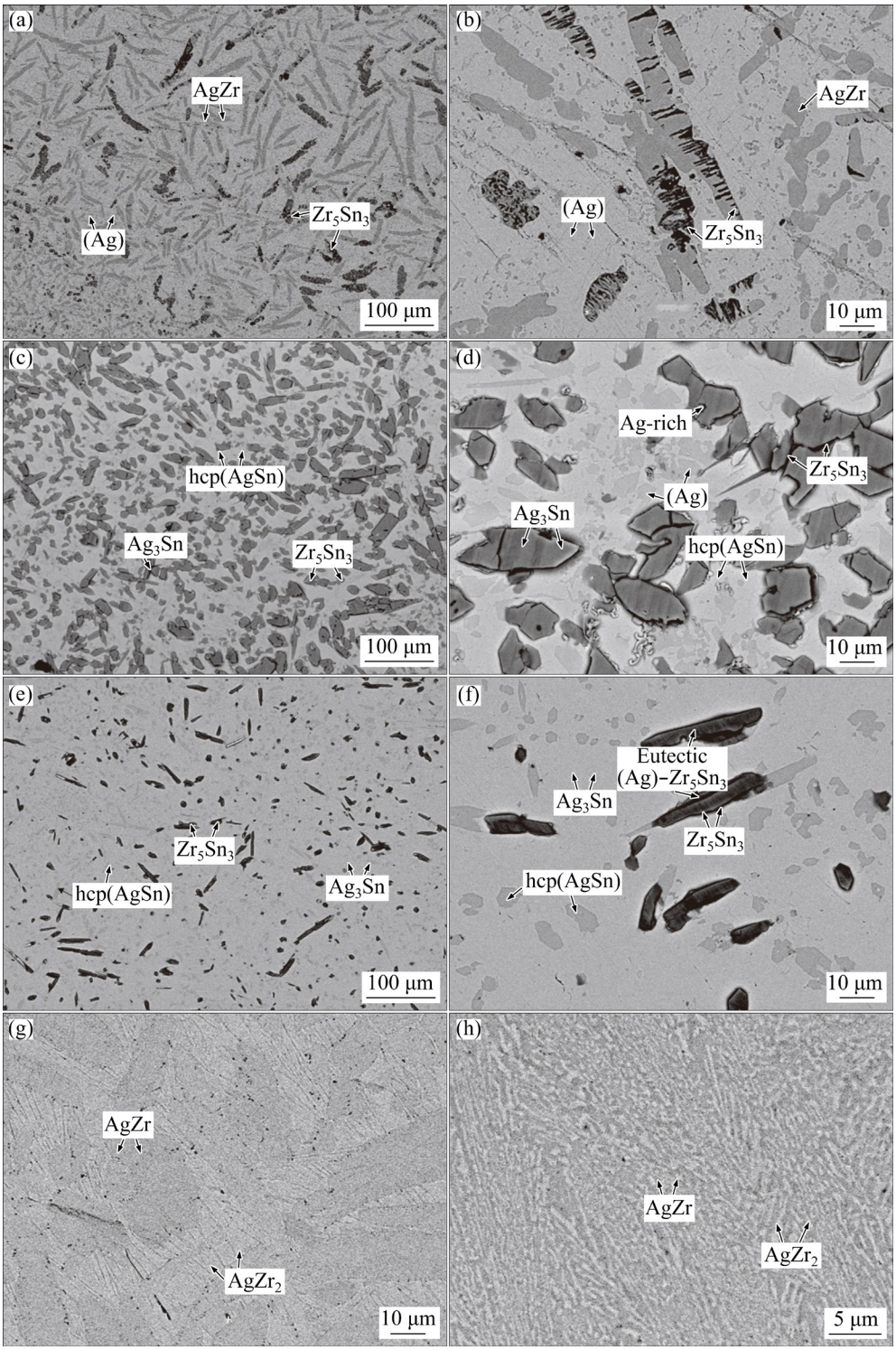

Fig. 8 BSE micrographs of as-cast alloys in Ag–Sn–Zr system: (a, b) Alloy D1 ($Ag_{83}Sn_2Zr_{15}$); (c, d) Alloy D5 ($Ag_{25}Sn_{35}Zr_{40}$); (e, f) Alloy D6 ($Ag_{25}Sn_{45}Zr_{30}$); (g, h) Alloy D7 ($Ag_{39}Sn_1Zr_{60}$)

the Zr_5Sn_3, AgZr and (Ag) phases, (Ag) is the most, followed by AgZr, and Zr_5Sn_3 is the least, which corresponds to the phases fraction, i.e., 76.22, 18.45 and 5.33 at.%, presented in Table S2 in Supplementary materials in detail. The calculated results are consistent with the observed ones shown in Figs. 8(a, b). The microstructures and solidification sequences of the as-cast alloy, D2 ($Ag_{86}Sn_2Zr_{12}$), are similar to those of Alloy D1. The solidification of Alloy D2 followed the path of the primary phase of Zr_5Sn_3, then the AgZr and (Ag) phases, and finally the eutectic microstructure, i.e.,

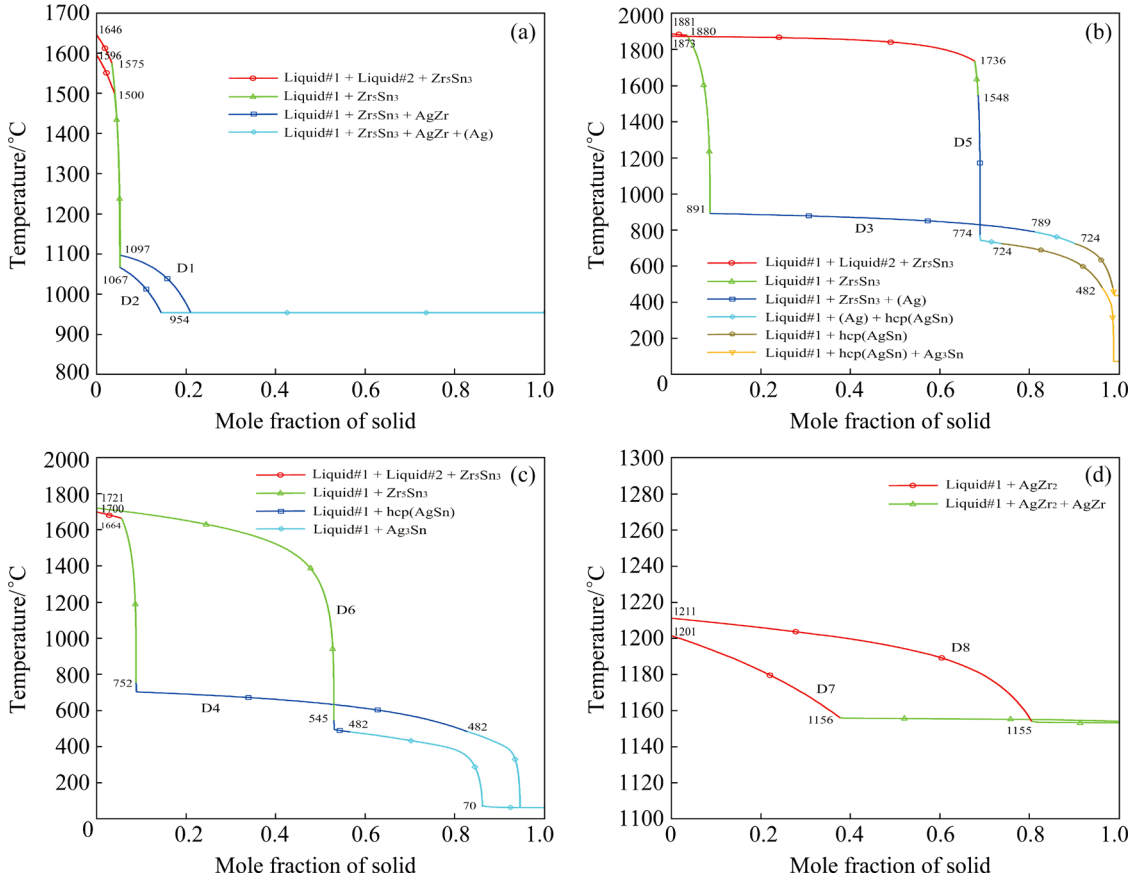

Fig. 9 Calculated Gulliver−Scheil solidification curves of as-cast alloys in Ag–Sn–Zr system: (a) Alloys D1 ($Ag_{83}Sn_2Zr_{15}$) and D2 ($Ag_{86}Sn_2Zr_{12}$); (b) Alloys D3 ($Ag_{85}Sn_{10}Zr_5$) and D5 ($Ag_{25}Sn_{35}Zr_{40}$); (c) Alloys D4 ($Ag_{70}Sn_{25}Zr_5$) and D6 ($Ag_{25}Sn_{45}Zr_{30}$); (d) Alloys D7 ($Ag_{39}Sn_1Zr_{60}$) and D8 ($Ag_{34}Sn_1Zr_{65}$)

Zr_5Sn_3 + AgZr + (Ag).

For the as-cast alloy, D5, there are four different phase regions, i.e., the white, light gray, dark gray and dark phase regions, in the solidified microstructure shown in Figs. 8(c, d), which correspond to hcp(AgSn), (Ag), Ag_3Sn and Zr_5Sn_3, respectively. As shown in Fig. 8(d), it also exists a small bright Ag-rich region embraced by the Zr_5Sn_3 phase which reveals the decomposition of one liquid phase into two liquid (Liquid → Liquid#1 + Liquid#2). According to the Gulliver−Scheil solidification curve of Alloy D5 shown in Fig. 9(b), the solidification path of Alloy D5 is as follows: Liquid → Liquid#1 + Liquid#2 + Zr_5Sn_3 → Liquid#1 + Zr_5Sn_3 → Liquid#1 + Zr_5Sn_3 + (Ag) → Liquid#1 + (Ag) + hcp(AgSn) → Liquid#1 + hcp(AgSn) → Liquid + hcp(AgSn) + Ag_3Sn. The primary crystallization phase for Alloy D5 is also Zr_5Sn_3. After the solidification of the primary phase, Alloy D5 undergoes an invariant reaction, i.e., Liquid + Zr_5Sn_3 + (Ag) → hcp(AgSn), then the peritectic reaction, i.e., Liquid + hcp(AgSn) → Ag_3Sn, and finally with the peritectic microstructure, i.e., hcp(AgSn) + Ag_3Sn. These simulated results are in accordance with the microstructure observed in the present experiment (see Figs. 8(c, d)). Figure 10(b) shows the mole fraction of the phases in Alloy D5 as a function of temperature during the solidification process. It can be seen that the Zr_5Sn_3 phase precipitates from the liquid phase starting at 1873 °C, then the (Ag), hcp(AgSn) and Ag_3Sn phases precipitate successively at about 1548, 774 and 482 °C, respectively. For mole fraction of the Zr_5Sn_3, (Ag), hcp(AgSn) and Ag_3Sn phases, Zr_5Sn_3 is the most, followed by hcp(AgSn) and (Ag), and Ag_3Sn is the least, which correspond to the phase fraction, i.e., 68.94, 23.89, 4.65 and 2.52 at.%, listed in Table S2 in Supplementary materials in detail. The calculated results are also consistent with the observed results shown in Figs. 8(c, d). The microstructures and solidification sequences of the as-cast alloy, D3 ($Ag_{85}Sn_{10}Zr_5$), are similar to those of Alloy D5. The solidification of Alloy D3 followed the path of the

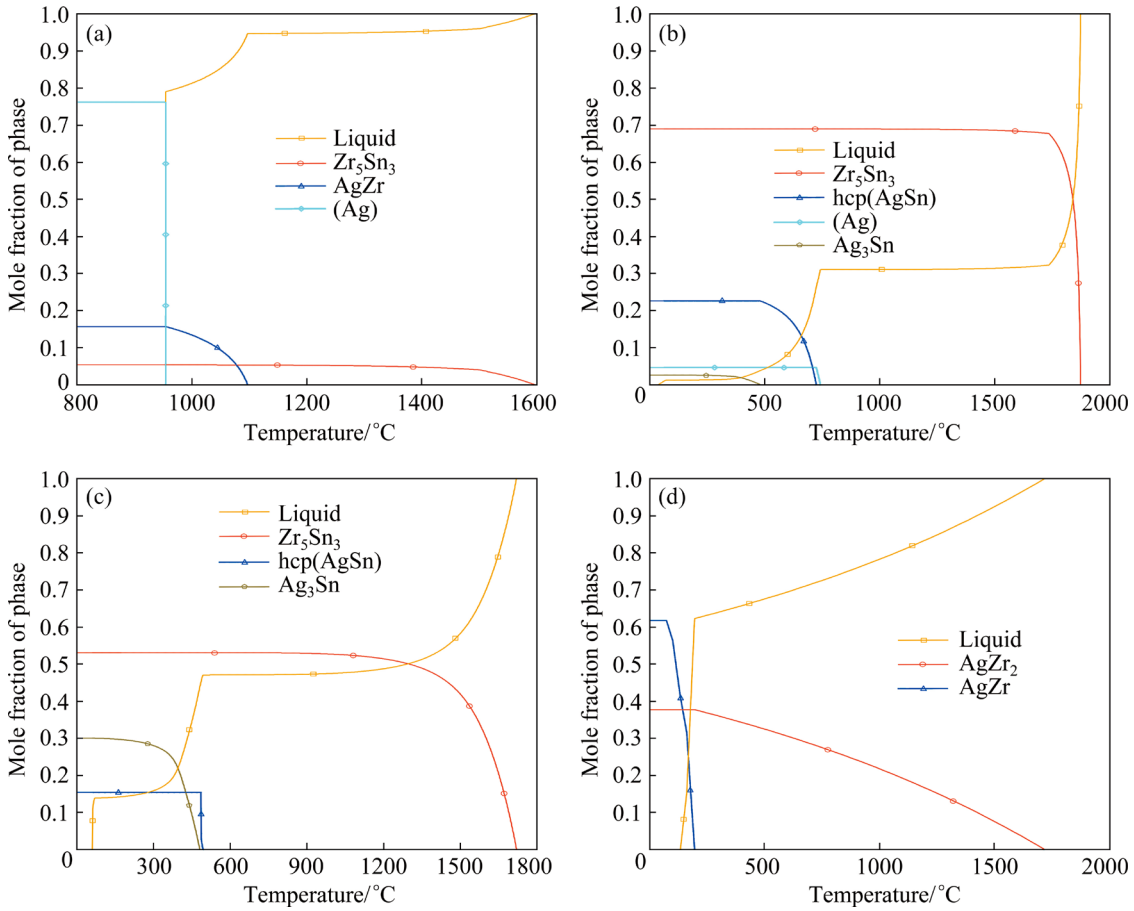

Fig. 10 Calculated mole fraction of phases vs temperature of as-cast alloys in Ag–Sn–Zr system: (a) Alloy D1 ($Ag_{83}Sn_2Zr_{15}$); (b) Alloy D5 ($Ag_{25}Sn_{35}Zr_{40}$); (c) Alloy D6 ($Ag_{25}Sn_{45}Zr_{30}$); (d) Alloy D7 ($Ag_{39}Sn_1Zr_{60}$)

primary phase of Zr_5Sn_3, then the (Ag), hcp(AgSn) and Ag_3Sn phases, and finally the peritectic microstructure, i.e., hcp(AgSn) + Ag_3Sn.

For the as-cast alloy, D6, there are three different phase regions, i.e., the white, gray and dark phase regions, in the solidified microstructure shown in Figs. 8(e, f), which correspond to (Ag), hcp(AgSn) and Zr_5Sn_3, respectively. Moreover, a eutectic (Ag) + Zr_5Sn_3 microstructure around the Zr_5Sn_3 phase is observed in Fig. 8(f). It is indicated that Alloy D6 undergoes the monotectic reaction Liquid#1 → Liquid#2 + Zr_5Sn_3 and one liquid phase is decomposed into two liquid (Liquid → Liquid#1 + Liquid#2). According to the Gulliver−Scheil solidification curve of Alloy D6 shown in Fig. 9(c), the solidification path of Alloy D6 is Liquid → Liquid#1 + Liquid#2 + Zr_5Sn_3 → Liquid#1 + Zr_5Sn_3 → Liquid#1 + hcp(AgSn) → Liquid + Ag_3Sn. The primary crystallization phase for Alloy D6 is also Zr_5Sn_3. After the solidification of the primary phase, Alloy D6 undergoes the peritectic reaction, i.e., Liquid + Zr_5Sn_3 → hcp(AgSn) and Liquid + hcp(AgSn) → Ag_3Sn, and ends with the Ag_3Sn phase. These simulated results are in accordance with the microstructure observed in the present experiment (see Figs. 8(e, f)). Figure 10(c) shows the mole fraction of the phases in Alloy D6 as a function of temperature during the solidification process. It can be seen that the Zr_5Sn_3 phase precipitates from the liquid phase starting at 1721 °C, and then the hcp(AgSn) and Ag_3Sn phases precipitate successively at about 545 and 482 °C, respectively. For mole fraction of the Zr_5Sn_3, hcp(AgSn) and Ag_3Sn phases, Zr_5Sn_3 is the most, followed by Ag_3Sn, and hcp(AgSn) is the least, which correspond to the phase fraction, i.e., 52.99, 29.96 and 17.05 at.%, presented in Table S2 in Supplementary materials in detail. The calculated results are also consistent with the observed results shown in Figs. 8(e, f). The microstructures and solidification sequences of the as-cast alloy, D4 ($Ag_{25}Sn_{35}Zr_{40}$), are similar to those of Alloy D6. The solidification of Alloy D4 followed the path of

the primary phase of Zr_5Sn_3, then the hcp(AgSn) and Ag_3Sn phases, and finally the Ag_3Sn phase.

For the as-cast alloy, D7, there are two different phases, i.e., the white and gray phases, in the solidified microstructure shown in Figs. 8(g, h), which correspond to $AgZr_2$, and AgZr, respectively. According to the Gulliver−Scheil solidification curve of Alloy D7 shown in Fig. 9(d), the solidification path of Alloy D7 is Liquid → Liquid#1 + $AgZr_2$ → Liquid#1 + $AgZr_2$ + AgZr. The primary crystallization phase for Alloy D7 is $AgZr_2$. After the solidification of the primary phase, Alloy D7 undergoes a eutectic reaction, i.e., Liquid → $AgZr_2$ + AgZr, and ends with the eutectic microstructure, i.e., $AgZr_2$ + AgZr. These simulated results are in accordance with the microstructure observed in the present experiment (see Figs. 8(g, h)). Figure 10(d) shows the mole fraction of the phases in Alloy D7 as a function of temperature during the solidification process. It can be seen that the $AgZr_2$ phase precipitates from the liquid phase starting at 1201 °C, and the AgZr phase precipitates successively at about 1156 °C. For mole fraction of the $AgZr_2$ and AgZr phases, AgZr is more than $AgZr_2$, which corresponds to the phase fraction, i.e., 62.29 and 31.71 at.%, presented in Table S2 in Supplementary material for detail. The calculated results are also consistent with the observed results shown in Figs. 8(g, h). The microstructures and solidification sequences of the as-cast alloy, D8 ($Ag_{34}Sn_1Zr_{65}$), are similar to those of Alloy D7. The solidification of Alloy D8 followed the path of the primary phase of $AgZr_2$, then AgZr phase, and finally the eutectic microstructure, i.e., $AgZr_2$ + AgZr.

It can be stressed that based on experiments and thermodynamic calculations, the Scheil solidification simulations and reaction scheme obtained from the thermodynamic parameters of the Ag–Sn–Zr system are anticipated to obtain the desired solidified microstructure and thus design a novel Ag-based and Zr-based alloy according to the relationship between microstructure and properties.

6 Conclusions

(1) The phase equilibria of the Ag–Sn–Zr system at 500, 700 and 900 °C were experimentally investigated by means of the XRD and SEM/EDS. Four three-phase regions and three two-phase regions at 500 °C, five three-phase regions and two two-phase regions at 700 °C and five three-phase regions and one two-phase region at 900 °C were determined. No ternary compound was found in the ternary system. The solubilities of Ag in Sn–Zr compounds, Sn in Ag–Zr compounds and Zr in Ag–Sn compounds were measured and their values are less than 3 at.% in general.

(2) The thermodynamic assessment of the Ag–Sn–Zr system was carried out by using the CALPHAD method based on the experimental data available in the present work. A set of thermodynamic parameters of the Ag–Sn–Zr system was obtained. The calculated isothermal sections are in good agreement with most of the reliable experimental data. The liquidus projection and reaction scheme of the Ag–Sn–Zr system over the whole composition were also presented.

(3) The microstructures of four as-cast alloys were measured by SEM/EDS and simulated under the Gulliver−Scheil non-equilibrium condition. The simulated results are consistent with the experimental data, which confirms that reliable thermodynamic parameters can describe the solidified microstructure well.

Acknowledgments

This work was supported by the Major Science and Technology Project of Precious Metal Materials Genetic Engineering in Yunnan Province, China (No. 202002AB080001), the National Natural Science Foundation of China (No. 52071002), and the Natural Science Foundation of Anhui Province, China (No. 2008085QE200).

Supplementary materials

Supplementary materials in this paper can be found at: http://tnmsc.csu.edu.cn/download/02-p1501-2021-1501-Supplemenary_materials.pdf.

References

[1] CHOI J, KWON S, PARK Y, KANG K, LEE H M. In silico high-throughput screening of Ag-based electrocatalysts for anion-exchange membrane fuel cells [J]. The Journal of Physical Chemistry Letters, 2021, 12(24): 5660−5667.

[2] WAN S, LIAO B K, DONG Z H, GUO X P. Comparative investigation on copper atmospheric corrosion by electrochemical impedance and electrical resistance sensors [J]. Transactions of Nonferrous Metals Society of China, 2021, 31(10): 3024−3038.

[3] HASANABADI M, SHAMSIPUR A, SANI H N,

OMIDVAR H, SAKHAEI S. Interfacial microstructure and mechanical properties of tungsten carbide brazed joints using Ag−Cu−Zn+Ni/Mn filler alloy [J]. Transactions of Nonferrous Metals Society of China, 2017, 27(12): 2638−2646.

[4] ZHANG B G, CHEN G Q, ZHANG C G, NI J Q. Structure and mechanical properties of aluminum alloy/Ag interlayer/steel non-centered electron beam welded joints [J]. Transactions of Nonferrous Metals Society of China, 2011, 21(12): 2592−2596.

[5] TAHER M, MAO F, BERASTEGUI P, ANDERSSON A M, JANSSON U. Tuning tribological, mechanical and electrical properties of Ag−X (X=Al, In, Sn) alloys [J]. Tribology International, 2018, 125: 121−127.

[6] NIYOMSOAN S, GARGARELLA P, CHOMSAENG N, TERMSUKSAWAD P, KÜHN U, ECKERT J. Phase separation in rapid solidified Ag-rich Ag−Cu−Zr alloys [J]. Materials Research, 2015, 18(Suppl 1): s120−s126.

[7] LIU J L, HE G Z, CALLOW A, LI K X, MOORE K L, NORDIN H, MOODY M, LOZANO-PEREZN S, GROVENOR C R M. The role of β-Zr in a Zr−2.5Nb alloy during aqueous corrosion: A multi-technique study [J]. Acta Materialia, 2021, 215(15): 117042.

[8] NI N, HUDSON D, WEI J, WANG P, LOZANO-PEREZ S, SMITH G D W, SYKES J M, YARDLEY S S, MOORE K L, LYON S, COTTIS R, PREUSS M, GROVENOR C R M. How the crystallography and nanoscale chemistry of the metal/oxide interface develops during the aqueous oxidation of zirconium cladding alloys [J]. Acta Materialia, 2012, 60(20): 7132−7149.

[9] CELTEK M, DOMEKELI U, SENGUL S, CANAN C. Effects of Ag or Al addition to CuZr-based metallic alloys on glass formation and structural evolution: A molecular dynamics simulation study [J]. Intermetallics, 2021, 128: 107023.

[10] LI B, SUN W C, QI H N, LV J W, WANG F L, MA M Z, ZHANG X Y. Effects of Ag substitution for Fe on glass-forming ability, crystallization kinetics, and mechanical properties of Ni-free Zr−Cu−Al−Fe bulk metallic glasses [J]. Journal of Alloys and Compounds, 2020, 827(25): 154385.

[11] YANG Y J, CHENG B Y, LV J W, LI B, MA M Z, ZHANG X Y, LI G, LIU R P. Effect of Ag substitution for Ti on glass-forming ability, thermal stability and mechanical properties of Zr-based bulk metallic glasses [J]. Materials Science and Engineering A, 2019, 746(11): 229−238.

[12] LIU Z K, WANG Y. Computational thermodynamics of materials [M]. Cambridge: Cambridge University Press, 2016.

[13] LUKAS H, FRIES S G, SUNDMAN B. Computational thermodynamics [M]. Cambridge: Cambridge University Press, 2007.

[14] VILLARS P, CALVERT L D. Pearson's handbook of crystallographic data [M]. American Society for Metals, Materials Park, 1991.

[15] CHEVALIER P Y. A thermodynamic evaluation of the Ag−Sn system [J]. Thermochimica Acta, 1988, 136: 45−54.

[16] KATTNER U R, BOETTINGER W J. On the Sn−Bi−Ag ternary phase diagram [J]. Journal of Electronic Materials, 1994, 23(7): 603−610.

[17] KARAKAYA I, THOMPSON W T. The Ag–Zr (silver−zirconium) system [J]. Journal of Phase Equilibria, 1992, 13(2): 143−146.

[18] KANG D H, JUNG I H. Critical thermodynamic evaluation and optimization of the Ag−Zr, Cu−Zr and Ag−Cu−Zr systems and its applications to amorphous Cu−Zr−Ag alloys [J]. Intermetallics, 2010, 18: 815−833.

[19] KWON Y U, CORBETT J D. Chemistry in polar intermetallic compounds. The interstitial chemistry of zirconium-tin (Zr_5Sn_3) [J]. Chemistry of Materials, 1992, 4(6): 1348−1355.

[20] TAN J Y, XU G L, TAO X M, CHEN F W, CUI Y W, ZHOU L. CALPHAD assessment of bio-oriented Ti−Zr−Sn system and experimental validation in Ti/Zr-rich alloys [J]. Calphad, 2019, 67: 101686.

[21] PETRENKO G J. On the alloying of silver with lead and tin [J]. Zeitschrift fur Anorganische Chemie, 1907, 53: 200−211.

[22] PUSHIN N A. Potential and nature of metallic alloys [J]. Zeitschrift fur Anorganische Chemie, 1908, 56: 20−22.

[23] MURPHY A J. The constitution of the alloys of silver and tin [J]. Journal of the Institute of Metals, 1926, 35: 107−129.

[24] NIAL O, ALMIN A, WESTGREN A. X-ray analysis of the systems: Gold–antimony and silver–tin [J]. Zeitschrift fur Physikalische Chemieabteilung B, 1931, 14: 83−94.

[25] FRANTIK R O, MCDONALD H J. A thermodynamic study of the tin-silver system [J]. Transactions of the Electrochemical Society, 1945, 88(1): 253.

[26] KARAKAYA I, THOMPSON W T. The Ag–Sn (silver−tin) system [J]. Bulletin of the Alloy Phase Diagrams, 1978, 8(4): 340−347.

[27] DINSDALE A T. SGTE data for pure elements [J]. Calphad, 1991, 15: 317−425.

[28] OH C S, SHIM J H, LEE B J, DONG NYUNG LEE. A thermodynamic study on the Ag–Sb–Sn system [J]. Journal of Alloys and Compounds, 1996, 238(1/2): 155−166.

[29] RAUB E, ENGEL M E. Alloys of zirconium with copper, silver and gold [J]. Zeitschrift fur Metallurgica, 1948, 39: 172−177.

[30] KARLSSON N, HARALDSEN H, FAURHOLT C. An X-ray study of the phases in the silver-zirconium system [J]. Acta Chemica Scandinavica, 1952, 6: 1424−1430.

[31] BETTERTON J O, EASTON J, EASTON D S. The silver-zirconium system [J]. Transactions of the Metallurgical Society of AME, 1958, 212: 470−475.

[32] LOBODA T P, PYATNITSKII V N, RAEVSKAYA M V, SOKOLOVSKAYA E M. Investigation of the zirconium-silver system by differential thermal analysis [J]. Vestnik Moskovskogo Universiteta, 1978, 19: 298−301.

[33] ZHANG K H, ZHAO H Z, ZHOU Y H. An investigation of the Ag−Zr phase diagram [J]. Journal of the Less Common Metals, 1988, 138(2): 173−177.

[34] MASSALSKI T B, OKAMOTO H, SUBRAMANIAN P R, KACPRZAK L. Ag−Zr (silver−zirconium) [M]. 2nd ed. Amsterdam: Materials Park, 1990: 117−119.

[35] HE X C, WANG H, LIU H S, JIN Z P. Thermodynamic description of the Cu−Ag−Zr system [J]. Calphad, 2006, 30: 367−374.

[36] HSIAO H M, LIANG S M, SCHMID-FETZER R, YEN Y W. Thermodynamic assessment of the Ag–Zr and Cu–Zr binary systems [J]. Calphad, 2016, 55: 77−87.

[37] MCPHERSON D J, HANSEN M. The system zirconium-tin [M]. Transactions Amsterdam, 1953, 45: 915−933.

[38] SPEICH G R, KULIN S A. The solid solubility of tin in alpha zirconium [R]. Pittsburgh: Westinghouse Electric Corp, 1952−09−23.
[39] GRAN G, ANDERSSON S, CYVIN S J, SKANCKE P N. The crystal structures of Zr_5Sn_3 and Zr_3Sn [J]. Acta Chemica Scandinavica, 1960, 14: 956−957.
[40] CARPENTER G J C, IBRAHIM E F, WATTERS J F. The aging response of zirconium−tin alloys [J]. Journal of Nuclear Materials, 1981, 102(3): 280−291.
[41] ABRIATA J P, BOLCICH J C, ARIAS D. The Sn–Zr (tin−zirconium) system [J]. Bulletin of Alloy Phase Diagrams, 1983, 4(2): 147−154.
[42] ARIAS D, ROBERTI L. The solubility of tin in α and β zirconium below 1000 ℃ [J]. Journal of Nuclear Materials, 1983, 118(2/3): 143−149.
[43] KWON Y U, CORBETT J D. The zirconium−tin system with particular attention to the Zr_5Sn_3–Zr_5Sn_4 region and Zr_4Sn [J]. Chemistry of Materials, 1990, 2(1): 27−33.
[44] MASCLET C T, BRACHET J C, SERVANT C, JOUBERT J M, BARBERIS P, DUPIN N, ZELLER P. Zirconium in nuclear industry [M]. 15th ed. ASTM Int. Symp: Sunriver, 2007.
[45] BAYKOV V I, PEREZ R J, KORZHAVYI P A, SUNDMAN B, JOHANSSON B. Structural stability of intermetallic phases in the Zr−Sn system [J]. Scripta Materialia, 2006, 55(5): 485−488.
[46] PÉREZ R J, TOFFOLON-MASCLET C, JOUBERT J M, SUNDMAN B. The Zr−Sn binary system: New experimental results and thermodynamic assessment [J]. Calphad, 2008, 32: 593−601.
[47] SHI C Y, LIU Y L, YANG B B, JIN B, HU B, RAJKUMAR V B, DU Y. Phase equilibria thermodynamics and solidified microstructure in the Ag–Cr–Zr system [J]. Journal of Alloys and Compounds, 2021, 863: 158618.
[48] QIU C L, HU B, ZHANG Y, WANG X Y, WANG Q P, MIN F F, DU Y. Experimental investigation and thermodynamic modeling of the Cu–Ag–Si ternary system [J]. The Journal of Chemical Thermodynamics, 2020, 150: 106172.
[49] ZHOU J Q, HU B, JIANG Y, QIU C L, DU Y, YIN H Q. Thermodynamic modeling of the Ag−X (X=B, Fe, Sm, Pu) binary systems [J]. Journal of Phase Equilibria and Diffusion, 2020, 41(3): 257−268.
[50] REDLICH O, KISTER A T. Thermodynamics of nonelectrolyte solutions *x–y–t* relations in a binary system [J]. Industrial & Engineering Chemistry, 1948, 40(2): 341−345.
[51] HILLERT M, STAFFANSSON L I. The regular solution model for stoichiometric phases and ionic melts [J]. Acta Chemica Scandinavica, 1970, 24: 3618−3626.
[52] SUNDMAN B, ÅGREN J. A regular solution model for phases with several components and sublattices suitable for computer applications [J]. Journal of Physics and Chemistry of Solids, 1981, 42(4): 297−301.
[53] SUNDMAN B, JANSSON B, ANDERSSON J O. The thermo-calc databank system [J]. Calphad, 1985, 9: 153−190.
[54] LUO Q, ZHAI C, SUN D K, CHEN W, LI Q. Interpolation and extrapolation with the CALPHAD method [J]. Journal of Materials Science & Technology, 2019, 35: 2115−2120.
[55] HU B, QIU C L, CUI S L, WANG P S, ZHOU J Q, XU W S, MIN F F, ZHAO J R. CALPHAD-type thermodynamic description of the phase equilibria in the Ti−W−M (M=Zr, Mo, Nb) ternary systems [J]. The Journal of Chemical Thermodynamics, 2019, 131: 25−32.
[56] XIE T C, SHI H, WANG H B, LUO Q, LI Q, CHOU K C. Thermodynamic prediction of thermal diffusivity and thermal conductivity in Mg−Zn−La/Ce system [J]. Journal of Materials Science & Technology, 2022, 97: 147−155.
[57] SCHEIL E. Comments on the transformation [J]. International Journal of Materials Research, 1942, 34(3): 70−72. (in German)
[58] ZUPANIČ F, NUNES C A, COELHO G C, CURY P L, LOJEN G, BONČINA T. Solidification of Be-free Ni-based dental alloy [J]. Transactions of Nonferrous Metals Society of China, 2018, 28(11): 2226−2235.

Ag−Sn−Zr 三元系的热力学模拟和凝固显微组织

张 宇[1]，胡 标[1]，石愈超[1]，刘树红[2]，杜 勇[2]，胡洁琼[3]

1. 安徽理工大学 材料科学与工程学院，淮南 232001；
2. 中南大学 粉末冶金国家重点实验室，长沙 410083；
3. 中国贵金属控股有限公司，昆明 650000

摘 要：采用关键实验和热力学模拟研究 Ag–Sn–Zr 三元系的相平衡。通过制备 22 个平衡合金，采用 X 射线衍射、扫描电子显微镜和能量色散 X 射线能谱测定 Ag–Sn–Zr 体系 500、700 和 900 ℃的等温截面。通过制备 8 个铸态合金，研究合金的凝固行为。测定 Zr、Sn 和 Ag 在 Ag–Sn、Ag–Zr 和 Sn–Zr 体系中二元化合物的溶解度，未发现三元化合物存在。基于 3 个边际二元系的热力学描述及获得的相平衡数据，采用 CALPHAD 方法对 Ag–Sn–Zr 体系进行热力学优化，得到一套自洽的热力学参数。计算的等温截面与实验数据吻合较好。计算和构筑 Ag–Sn–Zr 体系在整个成分范围内的液相面投影图和希尔反应图，模拟 Gulliver−Scheil 非平衡条件下铸态合金的凝固行为。模拟结果与实验数据相一致。

关键词：Ag–Sn–Zr 体系；相平衡；热力学模型；显微组织；凝固模拟

(Edited by Bing YANG)